To cite this version :

Simulation of Grain Refinement Induced by High-Speed Machining of OFHC Copper Using Cellular Automata Method

Jun Zhang[1]
State Key Laboratory for Manufacturing Systems Engineering,
Xi'an Jiaotong University,
Xi'an 710054, Shaanxi, China
e-mail: junzhang@xjtu.edu.cn

Xiang Xu
State Key Laboratory for Manufacturing Systems Engineering,
Xi'an Jiaotong University,
Xi'an 710054, Shaanxi, China;
Arts et Metiers Institute of Technology,
LaBoMaP,
HESAM University,
Rue Porte de Paris 71250, Cluny, France
e-mail: xuxiang@stu.xjtu.edu.cn

José Outeiro
Arts et Metiers Institute of Technology,
LaBoMaP,
HESAM University,
Rue Porte de Paris 71250, Cluny, France
e-mail: jose.outeiro@ensam.eu

Hongguang Liu
State Key Laboratory for Manufacturing Systems Engineering,
Xi'an Jiaotong University,
Xi'an 710054, Shaanxi, China
e-mail: 342723778@qq.com

Wanhua Zhao
State Key Laboratory for Manufacturing Systems Engineering,
Xi'an Jiaotong University,
Xi'an 710054, Shaanxi, China
e-mail: whzhao@xjtu.edu.cn

During high-speed machining (HSM), the microstructure of materials evolves with significant plastic deformation process under high strain rate and high temperature, which affects chip formation and material fracture mechanisms, as well as surface integrity. The development of models and simulation methods for grain refinement in machining process is of great importance. There are few models which are developed to predict the evolution of the grain refinement of HSM in mesoscale with sufficient accuracy. In this work, a cellular automata (CA) method with discontinuous (dDRX) and continuous (cDRX) dynamic recrystallization (DRX) mechanisms is applied to simulate the grain refinement and to predict the microstructure morphology during machining oxygen-free high-conductivity (OFHC) copper. The process of grain evolution is simulated with the initial conditions of strain, strain rate, and temperature obtained by finite element (FE) simulation. The evolution of dislocation density, grain deformation, grain refinement, and growth are also simulated. Moreover, cutting tests under high cutting speeds (from 750 m/min to 3000 m/min) are carried out and the microstructure of chips is observed by electron backscatter diffraction (EBSD). The results show a grain refinement during HSM, which could be due to the occurrence of dDRX and cDRX. High temperature will promote grain recovery and growth, while high strain rate will significantly cause a high density of dislocations and grain refinement. Therefore, HSM contributes to the fine equiaxed grain structure in deformed chips and the grain morphology after HSM can be simulated successfully by the CA model developed in this work. [DOI: 10.1115/1.4047431]

Keywords: high-speed machining, cellular automaton, dynamic recrystallization, grain refinement, machining processes, modeling and simulation

1 Introduction

High-speed machining (HSM) has been widely used due to its advantages of low cutting forces, small thermal deformation, high material removal rates, and low cost [1,2]. High-speed machining is a highly nonlinear thermal–mechanical coupling process, in which the microstructure in the deformation zone is altered under high strain rate, complex state of stress, and relatively high temperature [3–5]. Consequently, the mechanical behavior of the work material is affected, which in turn affects the quality of machined surface, the wear resistance, and fatigue life of workpiece [3,6,7]. With the rapid improvement of material microscopic testing technique and experimental methods, metallurgical structure and grain size are found to be the key factors influencing the mechanical behavior of the work material in machining, thus the chip formation process and surface quality. So, the microstructure is the indispensable link to establish the relationship between machining deformation parameters and physical and mechanical properties of materials [8–10]. However, the mechanism of microstructural evolution has not been fully revealed at present, so the model that can accurately reflect and predict microstructural evolution is of great significance for characterizing variation of materials properties and building connection between surface integrity and machining process.

By means of advanced material testing techniques, such as electron backscatter diffraction (EBSD), X-ray diffraction, and transmission electron microscope, several researches have investigated the evolution of grain structure and grain size with different deformation conditions and machining parameters [11–13]. A great number of studies have shown that the grain refinement induced by machining process has remarkable influence on the strength and hardness of materials [8–10]. Moreover, the grain refinement of machined surface under extrusion of tool clearance face could generate ultrafine grains even nanoscale grains, which results in the appearance of white layers [14–16]. The microstructure alterations, including grain refinement, deformation twining, and phase transformation, would lead to the increasing of microhardness and flow stress in machining process [17]. Besides that, the tribology behavior in machining process also strongly depends on microstructure property of materials [18]. The application of microstructure-based flow stress model has significant improvement of numerical simulation accuracy in predicting mechanical process [19]. In order to accurately predict microstructural evolution and study its effect on cutting process, the development of microstructure numerical model related to machining process has made great progress in recent years. Based on Estrin and Kim's dislocation density-based grain refinement material model [20], a finite element (FE) model that can predict dislocation density and grain size distribution in deformation zone has been developed and verified to be suitable for machining simulation of many kinds of materials [21,22], including the oxygen-free high-conductivity (OFHC) [9]. Recent studies have identified that the grain refinement of many

---

materials is mainly resulted from the dynamic recrystallization (DRX) behavior during machining process [23,24]. Based on Johnson-Mehl-Avrami-Kolmogorov DRX model, the evolution of grain size and microhardness induced by DRX can be simulated and predicted [25–27]. The development of models for grain refinement in machining process has made advances. However, the current models are based on the assumption of the homogenization of microstructural parameters. Although these models have access to present the distribution of dislocation density and grain size in macroscale, the disadvantage of these models is that they cannot reflect the grain refinement evolution process in mesoscale and show the final deformed and refined microstructure characteristics.

In studying of microstructure evolution under large plastic deformation, Goetz and Seetharaman established a dislocation density evolution model to simulate the grains nucleation and growth process induced by DRX [28]. Ding and Guo studied the DRX phenomenon of OFHC copper under low strain rate thermoplastic deformation and proposed a theoretical model of grain nucleation and growth and grain boundary migration to analyze the effect of temperature and initial grain size on the DRX process [29]. Based on these dislocation density and grain evolution theories, cellular automata (CA) method has been applied successfully in many researches to simulate the DRX process for various materials [30–32]. Therefore, based on the physical mechanism of dislocation and grain evolution, the CA method is an available way to conduct simulation of microstructure evolution under thermoplastic deformation in mesoscale. Few researches have investigated the microstructure evolution in machining process by using CA method. In addition, existing CA models are generally based on the discontinuous dynamic recrystallization theory [33], which has a lot of limitations for HSM with high strain rate and large deformation. Studies have shown that the dDRX behavior could be inhibited by high strain rate, and the cDRX begins to play a more important role gradually [34,35]. So far, a great number of studies have shown that the grain refinement induced by machining process has remarkable influence on the strength and hardness of materials. However, there are few models developed to predict the evolution of the grain refinement of machining process in mesoscale with sufficient accuracy. Few researches investigated the microstructure evolution in cutting process by using CA method. In this work, the application of CA method in cutting leads a new approach to simulate the microstructure morphology during machining OFHC copper. In addition, considering the effect of high strain rate of HSM on microstructure evolution, continuous dynamic recrystallization model is added for the first time to conduct CA simulation and the model combining cDRX and dDRX can simulate the microstructure of deformation zone of HSM more accurately.

To investigate the effect of DRX on grain refinement of materials during HSM of OFHC copper, a typical face-centered cubic single phase material is selected to study microstructure evolution without considering the effect of phase transformation. In this paper, the CA model combing cDRX and dDRX is established to study the effect of high temperature, large deformation, and high strain rate of HSM on microstructure evolution. FE simulation was first carried out to obtain the deformation parameters of HSM, and then based on these parameters CA method was used to simulate the microstructure evolution process. Besides that, the HSM experiments and microstructure observations were conducted to verify accuracy of the CA model. Finally, the influence of deformation parameters on microstructure evolution and final grain characteristics is analyzed with the cutting speed increasing.

2 Experimentation and Finite Element Simulation of High-speed Machining

2.1 Experimental Cutting Tests.
Dry cutting condition and cemented carbide inserts (model: SandvikN331.1A) were used in the machining tests. A milling cutter with a diameter of 80 mm and a helix angle of 0 deg was used by up milling to reach orthogonal high cutting speeds. Tool geometry was represented by a rake angle γ_0 of 0 deg, a clearance angle α_0 of 15 deg, and a tool edge radius r_n of 10 μm. The thickness and width of workpiece were 3 mm and 20 mm, respectively. The width of the workpiece is designed to be only a quarter of the tool diameter to avoid significant changes in cutting thickness, so the cutting thickness here is assumed to be constant. The axis of the cutter is kept aligning with the left edge of workpiece. As shown in Fig. 1, the geometry of the workpiece is specially designed by the Buda's method [36]. The workpiece including several holes with a dimension of 3 mm × 3 mm was adopted to realize quick-stop and obtain chip roots. The total cutting length for one feed is about 31 mm. As shown in Fig. 2, the cutting experiments were carried out on a five-axis machine center (Model: DMU 50). The milling tools were redesigned to realize orthogonal cutting. The main cutting edge of inserts was vertical to cutting plane and the rake face of inserts coincided with the axis of cutter. During the cutting process, cutting forces were measured by a piezoelectric dynamometer (Model: Kistler 9265B), and chip root samples were obtained to measure the shear angle. The thermal, mechanical, and physical properties of both workpiece and tool are listed in Table 1.

Table 2 shows the cutting parameters with the rotation speed varying from 3000 to 12000 rpm, a constant feed per tooth of 0.15 mm/z, the cutting feed varying from 450 to 1800 mm/min, and the cutting speed varying from 750 to 3000 m/min. Chips obtained at various cutting speeds are collected for further microstructure analysis by EBSD.

2.2 Finite Element Simulation.
To predict the distributions of strain, strain rate, and temperature, a 2D FE model of orthogonal cutting for plane strain condition was developed and schematically represented in Fig. 4. The constitutive material model proposed by Johnson–Cook [37] describes the material flow stress in function of the strain, strain rate, and temperature was used and is given by the following equation:

$$\sigma = (A + B\varepsilon^n)\left(1 + C\ln\left(\frac{\dot{\varepsilon}}{\dot{\varepsilon}_0}\right)\right)\left[1 - \left(\frac{T - T_0}{T_m - T_0}\right)^m\right] \quad (1)$$
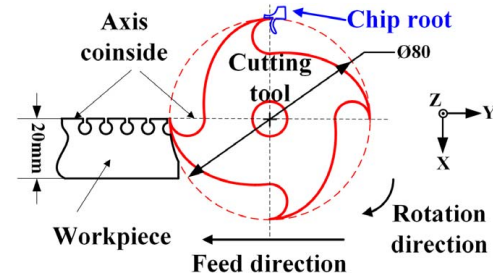

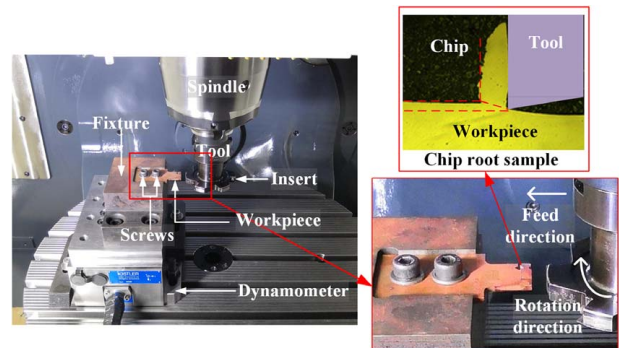**Fig. 1 Schematic of Buda's experimental method [36]**

Fig. 2 Experimental setup for high-speed orthogonal cutting of OFHC copper

Table 1 Material properties of OFHC copper and cutting tool

Material	Density (kg/m³)	Elastic modulus (GPa)	Poisson's ratio	Specific heat (J/(kg K))	Thermal conductivity (W/(m K))	Thermal expansion (K⁻¹)
Tool	11,900	534	0.22	400	50	–
OFHC	8960	124	0.34	380	401	1.65×10^{-5}

Table 2 Cutting parameters of HSM tests

Rotation speed (rpm)	Feed (f_z) (mm/z)	z (number of teeth)	Cutting feed (V_f) (mm/min)	v_c (m/min)
3000			450	750
6000	0.15	1	900	1500
9000			1350	2250
12,000			1800	3000

where σ is flow stress, ε and $\dot{\varepsilon}$, respectively, are equivalent plastic strain and strain rate, T is instantaneous temperature. $\dot{\varepsilon}_0$ is the reference strain rate, T_r and T_m are room and melted temperature, respectively. A, B, n, C, and m are material constants, which is strongly dependent on the condition of split Hopkinson pressure bar test. The values of the coefficients of this model for the OFHC copper are specified in Table 3.

In order to realize the material failure and chip separation process of machining, the node separation and element deletion technique are specified. In this study, an energetic-based ductile fracture criterion is applied, in which two stages, i.e., damage initiation and damage evolution, are included.

The damage initiation is described by the variable w, which is defined as

$$w = \sum \frac{\Delta \bar{\varepsilon}^{pl}}{\bar{\varepsilon}_0^{pl}} \tag{2}$$

where $\bar{\varepsilon}_0^{pl}$ is the equivalent plastic strain of damage initiation, $\Delta \bar{\varepsilon}^{pl}$ is equivalent plastic strain. And $\bar{\varepsilon}_0^{pl}$ can be calculated by the following equation, which is dependent on stress triaxiality, strain rate, and temperature

$$\bar{\varepsilon}_0^{pl} = \left[D_1 + D_2 \exp\left(D_3 \frac{\sigma_p}{\bar{\sigma}}\right) \right] \left[1 + D_4 \ln\left(\frac{\dot{\bar{\varepsilon}}}{\dot{\bar{\varepsilon}}_0}\right) \right] \left[1 + D_5 \frac{T - T_r}{T_m - T_r} \right] \tag{3}$$

where parameters $D_1 - D_5$ are the JC damage constant, which is given in Table 4.

As shown in Fig. 3, w increases continuously with plastic deformation, and when w reaches a critical value of 1, damage evolution

is activated. In the stage of damage evolution, the fracture energy is obtained by integrating yield stress with plastic deformation and it can be described as

$$G_f = \int_{\bar{\varepsilon}_0^{pl}}^{\bar{\varepsilon}_f^{pl}} L\sigma_y d\bar{\varepsilon}^{pl} = \int_0^{\bar{u}_f^{pl}} \sigma_y d\bar{u}^{pl} \tag{4}$$
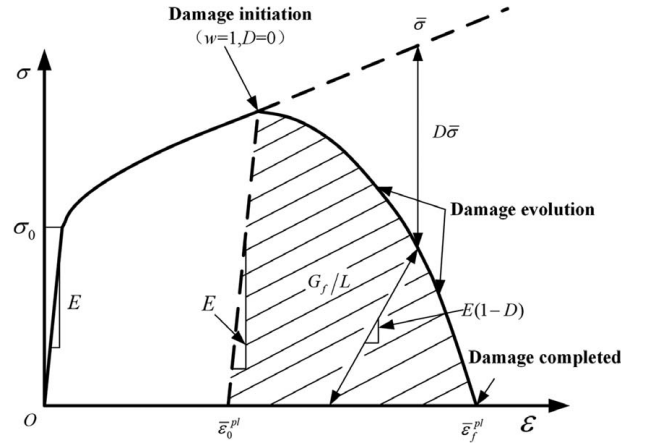
where L is the characteristic length, $\bar{u}^{pl}$ is equivalent displacement, and $\bar{u}_f^{pl}$ is equivalent displacement at failure.

According to the research of Mabrouki et al. [39], the fracture energy G_f can be calculated by fracture toughness K_C as
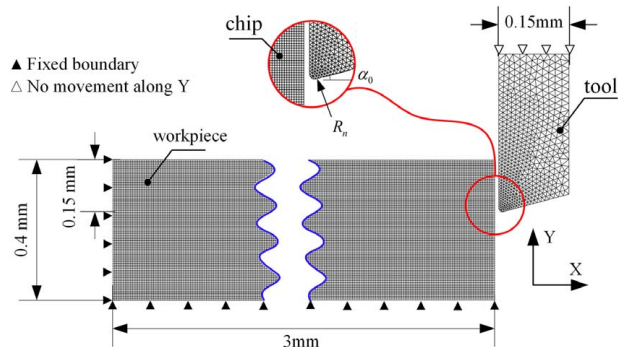
$$G_f = \left(\frac{1 - v^2}{E}\right) K_C^2 \tag{5}$$

The stiffness degradation of materials in condition of damage evolution can be described by variable D, and when D increase from 0 to 1, the damage evolution process completes

$$D = \frac{L\bar{\varepsilon}}{\bar{u}_f^{pl}} = \frac{\bar{u}}{\bar{u}_f^{pl}} \tag{6}$$

Fig. 3 Stress–strain curve of material damage degradation

Table 3 JC parameters of the OFHC copper used in the simulations [37]

Parameters	A (MPa)	B (MPa)	n	m	C	$\dot{\varepsilon}_0$ (1/s)	T_m (K)	T_0 (K)
Value	90	292	0.31	1.09	0.025	1	1356	293

Table 4 JC damage constant of OFHC copper [38]

D_1	D_2	D_3	D_4	D_5
0.54	4.89	−3.03	0.014	1.12

Fig. 4 Mesh and boundary conditions of the orthogonal cutting model

Table 5 Comparison of simulated and experimental cutting force

Cutting speed (m/min)	Simulated force F_t (N) Average	Experimental force F_t (N) Average	Error (%)
$V = 750$	612.4	634.4	3.5
$V = 1500$	639.0	663.3	3.7
$V = 2250$	723.0	714.5	1.2
$V = 3000$	817.9	748.7	9.2

Table 6 Shear angle and CCR obtained from experiments and simulations

Cutting speed (m/min)	Average experimental results		Average simulation results		Error (%)
	Shear angle (deg)	CCR	Shear angle (deg)	CCR	
$V = 750$	13.6	4.13	15.1	3.71	10.2
$V = 1500$	15.8	3.53	16.9	3.29	6.8
$V = 2250$	17.7	3.1	18.3	3.02	2.6
$V = 3000$	18.3	3	19.2	2.87	4.3

where equivalent displacement $\bar{u} = L\bar{\varepsilon}$ and equivalent displacement at failure $\bar{u}_f^{pl} = 2G_f/\sigma_{y0}$.

The cutting process with several cutting speeds ($v_c = 750$, 1500, 2250, 3000 m/min) is simulated by finite element analysis in ABAQUS/Explicit. Tool geometry and material is the same with the experiments. The mesh approach and boundary conditions of the orthogonal cutting model are shown in Fig. 4. Four-node quadrilateral continuum elements (CPE4RT) with reduced integration and hourglass control features are used to mesh the workpiece for a coupled displacement–temperature analysis. A constant uncut chip thickness of 0.15 mm and cutting width of 3 mm were used in the simulations. Three-node linear displacement and temperature elements (CPE3T) with plane strain feature are chosen to mesh the

tool. Reducing mesh size gradually is considered as an effective way to balance calculation accuracy and efficiency. The mesh size of the uncut chip and sacrificial layer is determined to be 5 μm. Besides that, the mesh size of tool in tool-chip contact zone is set less than that of workpiece. The total number of elements of tool and workpiece are 48,000 and 1339. The workpiece is fixed on the bottom and left side and the tool is moving in the X-direction only, from right to left at constant cutting speed. The length of the cutting path is set to be 2.2 mm to achieve the steady state. The initial temperature of the workpiece and tool was set to 20 °C.

The stick-slip friction contact model proposed by Zorev is used [40], which can be represented by the following equation:

$$\tau_f = \begin{cases} \tau_Y, & \mu\sigma_n \geq \tau_Y \quad \text{(sticking region)} \\ \mu\sigma_n, & \mu\sigma_n \geq \tau_Y \quad \text{(sliding region)} \end{cases} \quad (7)$$

where μ is the Coulomb friction coefficient with a value of 0.3 adopted in this study, σ_n is the normal stress. The yield shear stress, τ_Y, is calculated by the estimated yield stress of the material of the chip, given by $\tau_Y = \sigma_Y/\sqrt{3}$.

To verify the accuracy of the FE machining model, the cutting tangential force and chip morphology obtained from simulation and experiments under different cutting speeds were selected to compare. When analyzing the experimental cutting force, to avoid the vibration of cutting force caused by the instability at the beginning and end of cutting process, the stable periods of cutting process were selected to calculate the average tangential forces. The comparison of simulated and experimental cutting force is listed in Table 5, from which it can be summarized that cutting forces obtained by experiment is slightly larger than the simulated value, and the error is less than 10% and within the reliable range.

The shear angle and chip compression ratio (CCR) is also taken into account to verify the accuracy of plastic deformation from simulation. The CCR was calculated by the ratio of the chip thickness to the uncut chip thickness [41]. It can be seen from Table 6 that the shear angle and CCR obtained by this model show a well agreement with experiments.

Figure 5 show the distributions of the equivalent plastic strain, strain rate, and temperature in the deformation zone at a cutting
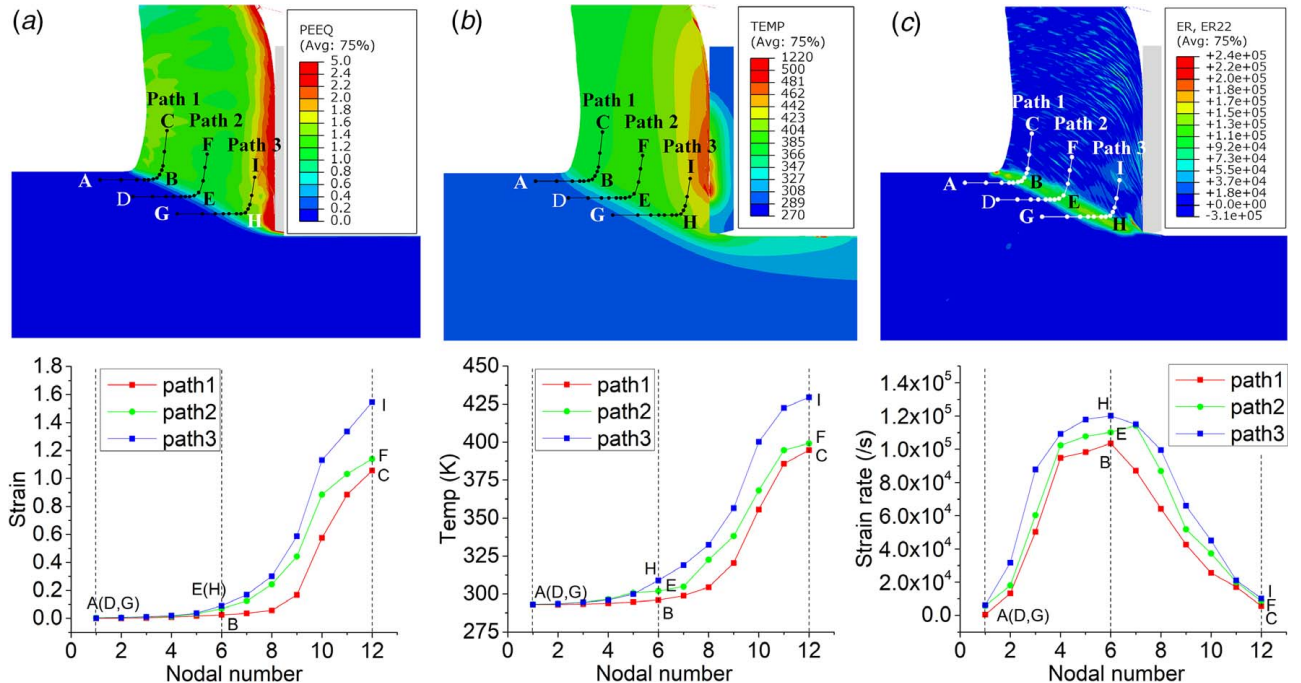
Fig. 5 Distributions of (a) strain, (b) temperature, and (c) strain rate along both chip free surface (path 1), middle area of chip (path 2), and chip surface in contact with the tool (path 3) for a cutting speed equal to 1500 m/min

Table 7 Maximum values of strain, strain rate, and temperature along path 3 in Fig. 5

v_c (m/min)	Strain	Temperature (K)	Strain rate (1/s)
750	1.6	435	6×10^4
1500	1.9	478	1.2×10^5
2250	2.2	486	3.6×10^5
3000	2.8	512	7.8×10^5

speed of 1500 m/min. The evolution of these variables is analyzed along both chip free surface, middle area of chip, and chip surface in contact with the tool. The strain in chip surface in contact with the tool reaches about 2.0, which is higher than 1.5 in the middle area of the chip and 1.0 of chip free surface due to the influence of tool-chip friction. The maximum of strain rate distributed along the shear plane is close to 10^6/s. In the second deformation zone, the temperature goes up significantly to about 480 K due to extrusion and friction of the cutting tool and reaches the critical temperature of DRX, which has great influence on the microstructure evolution. Generally, the severe plastic deformation has the characteristics of high strain rate and high temperature during HSM.

Then, the maximum values of strain, strain rate, and temperature obtained along the chip surface in contact with the tool (path 3) are extracted and represented in Table 7. The CA simulation of microstructure evolution from Samanta et al. [42] showed that the simulated microstructure depended on the thermomechanical loading condition and the accurate acquisition of strain rate and temperature was the key to conduct a reliable CA simulation. So these values in Table 7 are used as input boundary conditions in the CA model for predicting DRX during HSM.

3 Theoretical Model for Dynamic Recrystallization

Dynamic recrystallization occurs only when the dislocation density in a deforming matrix reaches a critical level, which depends on physical deformation parameters, such as strain, strain rate, and temperature during HSM. DRX includes two types: dDRX and cDRX. Two important aspects of dDRX are nucleation and grain growth based on grain boundary migration while cDRX appears as lattice rotation and grain subdivision, as shown in Fig. 6. In order to simplify the analysis, two assumptions are proposed here.

(1) Initial dislocation density ρ_{ini} in the matrix material is uniform and when it reaches a critical value, nucleation of dDRX occurs. For the new recrystallization grains (R-grains), the dislocation density evolves from initial dislocation density. The grains are set with an initial dislocation density of 10^9/m^2, representative for the annealed and undeformed state [45]. Corresponding to the grain boundary bulging nucleation mechanism, dDRX nucleate at both initial grain boundaries and R-grain boundaries.

(2) For OFHC copper, dislocation cross-slip and low angle boundaries are easily observed during hot deformation, especially at high strain rate and large strain, and cDRX occurs when the critical dislocation density is achieved. Equiaxed recrystallization grains with high orientation angle are transformed from deformation substructures by lattice rotation [46]. In this paper, assume that a grain is divided into three grains with 120 deg.

3.1 Dislocation Density. Dislocation density plays an important role in microstructure evolution, which is temperature and strain rate dependent. The dependence of the dislocation density $\rho_{x,y}$ at the site (x, y) on the shear strain ε is given by

$$\frac{d\rho_{x,y}}{d\varepsilon} = k_1 \sqrt{\rho_{x,y}} + k_2 \rho_{x,y} \tag{8}$$

which is the Kocks and Mecking (KM) law [47], where k_1 is a constant that represents hardening and k_2 is the softening parameter representing the recovery of dislocations. The high-temperature flow stress is related to the average dislocation density $\bar{\rho}$ by

$$\sigma = \alpha \mu b \sqrt{\bar{\rho}} \tag{9}$$

where α is a dislocation–interaction term, which is 0.5 for most metals, μ is the shear modulus, and b is Burger's vector.

The values of k_1 and k_2 are required from stress–strain curve. k_2 is strongly dependent on the condition of strain rate and temperature. k_1 is related to k_2 and saturated stress σ_s. k_1 and k_2 can be determined by following equations [48]:

$$\sigma = \sigma_s [1 - \exp(-k_2 \varepsilon)]^{1/2} \tag{10}$$
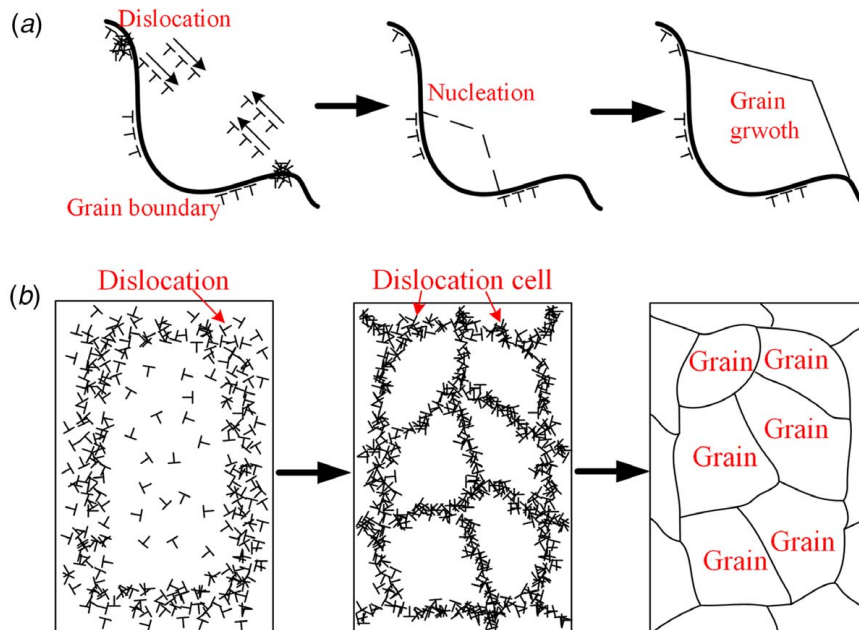
Fig. 6 Mechanisms of (a) dDRX process [43] and (b) cDRX process [44]

Table 8 The values of k_1 and k_2 at different cutting speeds

Cutting speed (m/min)	750	1500	2250	3000
k_1	9.21×10^8	8.87×10^8	8.54×10^8	7.92×10^8
k_2	4.62	4.55	4.44	4.22

$$k_1 = k_2 \left(\frac{\sigma_s}{\alpha \mu b} \right)^2 \tag{11}$$

According to the condition of strain rate and temperature and stress–strain curve at different cutting speeds, the values of k_1 and k_2 at different cutting speed are listed in Table 8.

The accumulation of dislocations could lead to DRX. Roberts and Ahlblom [49] have proposed that the critical dislocation density ρ_{cr} depends on deformation conditions and can be calculated after considering the free energy change according to the following equations:

$$\rho_{cr} = \left(\frac{20\gamma\dot{\varepsilon}}{3blM\tau^2} \right)^{1/3} \tag{12}$$

$$\tau = c_2 \mu b^2 \tag{13}$$

$$\frac{\sigma l}{\mu b} = K_1 \tag{14}$$

where γ is the grain boundary energy, $\dot{\varepsilon}$ is strain rate, l is the dislocation mean free path, M is the grain boundary mobility, τ is the dislocation line energy, c_2 is a constant of 0.5, and K_1 is a constant which is about 10 for most metals.

3.2 Nucleation and Growth of dDRX.

The nucleation rate P_d for dDRX is a function of both the temperature T and the strain rate $\dot{\varepsilon}$ and can be described by the following equation proposed by Kugler and Turk [50]

$$P_d = C\dot{\varepsilon} \exp\left(-\frac{Q_a}{RT} \right) \Delta t \tag{15}$$

where C is a constant of 1, Q_a is the activation energy, R is the gas constant, and Δt is time-step.

The growth driving force of an R-grain comes from the reduction of storage energy, or in other words the difference of dislocation densities between the R-grain and the matrix. It is assumed that the growth velocity V_i of the ith R-grain is directly proportional to the mobility of the boundary and driving force per unit area, thus

$$V_i = \frac{\lambda M F_i}{4\pi r_i^2} \tag{16}$$

where λ is a constant of 1, r_i is the radius of the ith R-grain. The mobility of grain boundary, M, is given by the following equation proposed by Stüwe and Ortner [51]

$$M = \frac{\delta D_{ob} b}{KT} \exp\left(-\frac{Q_b}{RT} \right) \tag{17}$$

where δ is the characteristic grain-boundary thickness, D_{ob} is the boundary self-diffusion coefficient, K is Boltzmann's constant, T is the temperature, Q_b is the boundary-diffusion activation energy, and R is gas constant.

If the R-grain is assumed spherical, the driving force F_i can be derived from the energy change of surface and volumetric energy given by the following equation [52]:

$$F_i = 4\pi r^2 \tau(\rho_m - \rho_d) - 8\pi r\gamma \tag{18}$$

where γ is the grain boundary energy which is dependent on the misorientation between neighboring grains, τ is the dislocation line energy, ρ_m and ρ_d are the dislocation density of the matrix and the R-grain.

3.3 Modeling of cDRX.

During large deformation, a large number of dislocation cell structures are generated with low dislocation density in cell interiors and high dislocation density at cell walls. The dislocation in cell interior continually migrates to cell walls resulting from high temperature of machining, and the increasing of dislocation density at cell walls gives rise to the formation of subgrains. Furthermore, the misorientations of subgrains gradually increase due to the rotation of grains, which can generate the fully recrystallized grains. According to Estrin and Vinogradov's model [53], the average cell size d_{cr} is inversely proportional to the square root of the total dislocation density $\bar{\rho}$, and combining with Eq. (9), the relationship between the average cell size and flow stress can be expressed by

$$d_{cr} = \frac{H_0}{\sqrt{\bar{\rho}}} = \frac{\alpha \mu b H_0}{\sigma} \tag{19}$$

where H_0 is a constant equal to 10 for OFHC copper [54]. This equation is based on the dislocation theory, in which the pile-up of dislocation can result in increasing of local dislocation density in grain interior, grain distortion, and grain refinement. It is worth noting that the propagation of dislocation in refined grains is of certain limitations so that the saturation of cDRX behavior will cause the grain size to reach the critical value. With the increasing of dislocation density, when the relationship between grain size and flow stress cannot satisfy Eq. (19), which means that current grain size d_i is greater than the critical grain size d_{cr}, cDRX process is carried out to conduct the segmentation and refinement of grains. The current grain size is calculated by the following equation [55]:

$$d_i = \sqrt{\frac{4N_i a^2}{\pi}} \tag{20}$$

where N_i is the lattice number that makes up the current grain, a is the lattice size. Considering the Hall–Petch relation between material strength and grain size [56,57], with the decreasing of grain size, the intense distribution of grain boundary with high energy induces the increasing of material strength, which makes grains harder to refine. Therefore, grain segmentations caused by cDRX was carried out with a probability (P_c), which can be calculated by following equation:

$$P_c = \frac{\omega d_i^2}{d_{ini}^2} \tag{21}$$

where ω is constant equal to 0.5, d_i and d_{ini} are current and initial grain size, respectively. The used material parameters in the CA simulation are listed in Table 9.

Table 9 Material parameters used in CA simulation

Variable	Q_a (kJ/mol)	Q_b (kJ/mol)	μ (MPa)	b (m)	γ (J/m^2)	R (J/(mol K))	δD_{ob} (m^3/s)	K (J/K)	ρ_{ini} (1/m^2)
Value	261	104	4.2×10^4	2.56×10^{-10}	0.5	8.314	5×10^{-15}	1.38×10^{-23}	1×10^9

4 Cellular Automata Simulation of Grain Evolution in Deformation Zone of Chip

4.1 Detailed Description of Cellular Automata Model for Dynamic Recrystallization.

Based on the above theoretical model of DRX, the routine has been developed in FORTRAN by following the CA transformation rules. The CA method is an algorithm describing the discrete spatial and/or temporal evolution in a complex physical system by applying a local deterministic or probabilistic transformation rule [58]. For the selection of lattice size and space, smaller lattice size requires more lattice number to describe the same spatial area, which helps improve the calculation accuracy but reduce the calculation efficiency. And the lattice size should be five times smaller than the final grain size in general and the whole spatial size should be at least twice bigger than the initial grain size. Based on these boundary conditions, several tests with different lattice numbers are conducted, and finally a 2D square lattice space with a size of 300×300 cells are determined to have a balance between calculation accuracy and efficiency, in which size of every lattice is $1\ \mu m \times 1\ \mu m$. Every lattice site has state variables: one dislocation density variable, one orientation variable, one status variable that indicates whether it is the matrix or R-grain, one status variable that judge whether it is the grain boundary, and one color variable that represents different grains. The von Neumann's neighboring rule which considers the nearest neighbors is selected and the value of a state variable at an arbitrary site (x, y) at a time $(t + \Delta t)$ can be expressed as

$$\psi_{x,y}^{t+\Delta t} = f(\psi_{x-1,y}^{t}, \psi_{x,y-1}^{t}, \psi_{x,y}^{t}, \psi_{x+1,y}^{t}, \psi_{x,y+1}^{t}) \qquad (22)$$

where $\psi_{x,y}^{t}$ represents the value of variable ψ at site (x, y) at time t. Function f is the transformation rule depending on the characteristics of the system, in which the relation indicates that the lattice state variable at next step is determined by the state variable of the lattice and of its four neighbors, as shown in Fig. 7.

In order to simulate the equiaxed growth of R-grains, the following probabilistic transformation rules are applied as

$$\begin{cases} F_i > 0 \\ \int_0^t v_i dt \geq a \end{cases} \qquad (23)$$

When the driving force F_i for the growth of the ith R-grain is positive, and the fraction of R-grain $\left(\int_0^t V_i dt / a\right)$ at time t is greater than or equal to one, the distance of grain boundary migration is greater than or equal to lattice size, where V_i is the growth velocity determined by Eq. (16), dt is the time-step, and a is the side length of one lattice. The time-step is the shortest growth time of a cell, which is calculated by the following equation:

$$dt = \frac{a}{V_{max}} = \frac{k_2^2 a}{M \tau k_1^2} \qquad (24)$$
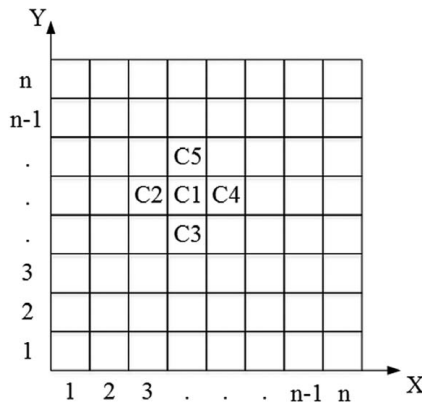
Fig. 7 Neighboring relationship of lattices in the cell space

The transformation probability is defined as $P_z = n_z/4$, where n_z is the number of transformed neighboring sites and 4 is the total number of von Neumann's neighboring sites. The average grain size is obtained by dividing the total area by the number of grains. The detailed steps are shown in Fig. 8 and described as follows:

(1) First step: generation of initial grains of matrix material

With the reference of the natural grain growth mode, the initial grains with random orientations are generated through seeding and grain growth process, in which the simulated annealing algorithm is adopted to reduce the energy of grain boundary in space [59]. The total energy is provided by the grain boundary in the CA space, and the energy of the interfacial cells depends on the number of the same state of central cell and neighboring cells. The reduction of the interfacial energy after the state transition is the driving force for the natural grain growth. The average grain size of initial grains of OFHC copper is determined by EBSD results, and the morphology of grains is set to be hexagon and equiaxed.

(2) Second step: evolution of dislocation density

The critical dislocation density, shear modulus, dislocation line tension, and grain boundary mobility were calculated based on the deformation parameters obtained from FE simulation, i.e., the strain, strain rate, and temperature. After total calculation time-step is determined, the dislocation density of each lattice will be updated in every time-step in turn according to the KM model in Sec. 3.1.

(3) Third step: grains nucleation and growth process of dDRX

After scanning the whole lattice space, when the dislocation density of a lattice is found to increase to the critical value, this lattice may transform as dDRX grain nuclei with probability P_d. If so, this lattice is marked as dDRX grain, and then its orientation changes randomly and its dislocation density is set to be initial value ρ_{ini}. As for the grain growth process of dDRX, when the status variables of a lattice satisfy the transformation rules in Eq. (23), the lattice may transform with probability P_z and marked as dDRX grain, and its orientation and dislocation density will be set as same as neighboring grain. The nucleation and growth process of dDRX is shown as Fig. 9.

(4) Fourth step: grains partition process of cDRX

By scanning the whole lattice space, when the size of a grain is greater than the critical grain size of cDRX, this grain may be patitioned with probability P_c, and the orientation of new produced grains is set as random value. The grain partition process of cDRX is displayed in Fig. 10.

(5) Fifth step: the loop and iteration process of CA simulation

Cellular automata simulation of microstructure evolution is conducted with the increasing of strain, in which time-step is $\Delta t = \varepsilon/(N\dot{\varepsilon})$, where N is the total iteration step, equal to 300 in this study. During each time-step, the whole lattice space is searched and related judgement and calculation are carried out to update the lattice state at the next step. The steps (2), (3), and (4) loop in every step until the predetermined deformation is achieved. After that, the results of dislocation density, grain size, grain distribution, and DRX characteristics will be output.

4.2 Microstructure Evolution at Various Cutting Speeds.

Without the effect of phase transformation, as a typical single phase material, OFHC copper is chosen for modeling to investigate the effect of DRX process on grain refinement. Strain, strain rate, and temperature obtained from finite element simulation of orthogonal cutting are used as input parameters of the CA model. Figure 11 shows the initial grain distribution with different orientations obtained by a natural grain growth algorithm. The coarse grains are just equiaxed with an average grain size of 107 μm, determined experimentally by EBSD.
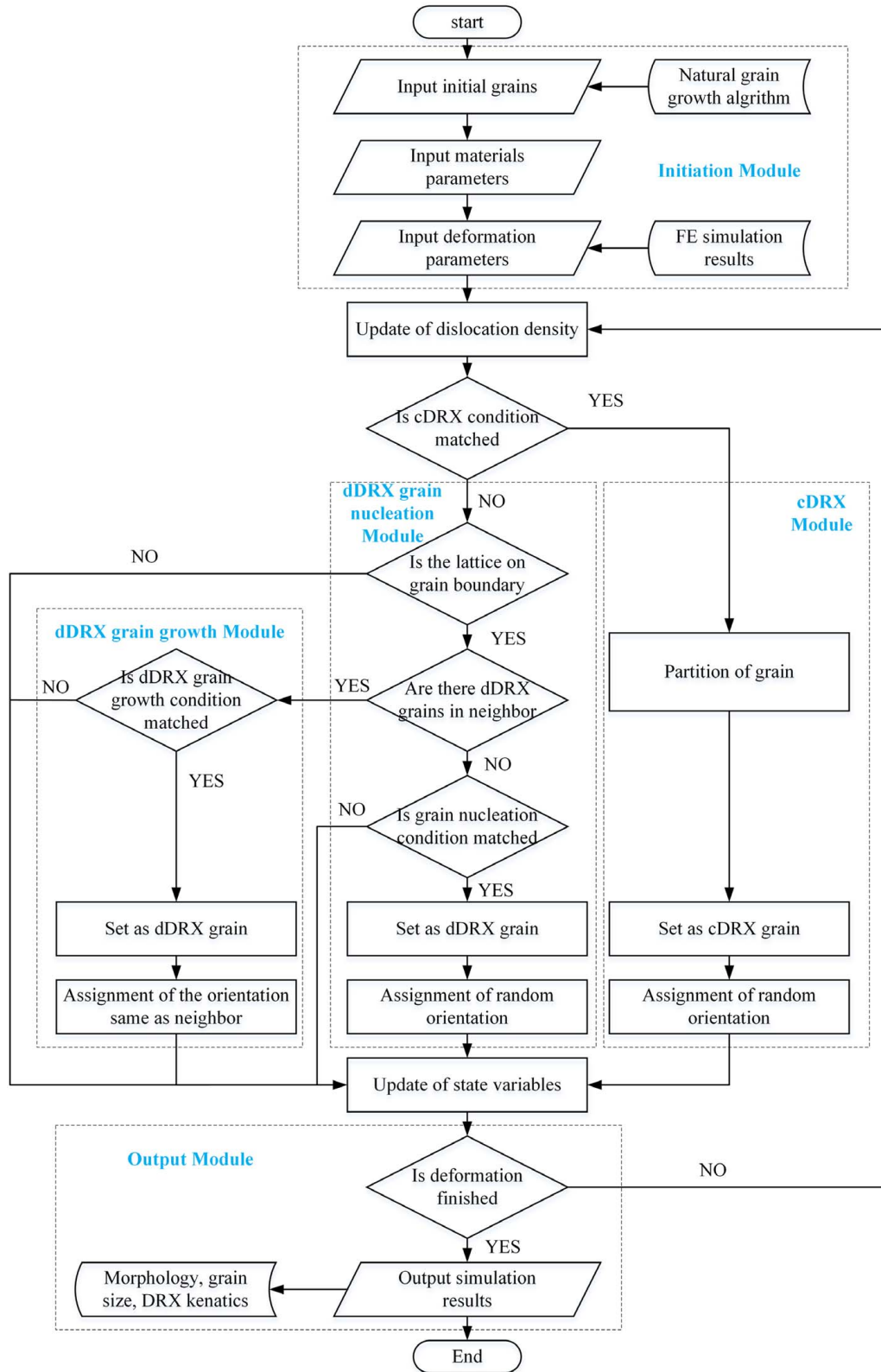
Fig. 8 **Flowchart of the loop and iteration process in CA simulation**

The final microstructure at the cutting speed of 3000 m/min is illustrated in Fig. 12. It is obviously seen that the final grain is no longer the initial coarse crystal after DRX, and almost all of it has been transformed into fine equiaxed grains. The original grain boundaries have disappeared and a large number of new grain boundaries are formed, which reflects the effect of DRX on refining grains. At the same time, the grains formed by different evolution mechanisms can be distinguished. There is not enough time for the nuclei at grain boundaries after dDRX to grow due to the high strain rate, so that these dDRX grains keep quite fine and are just composed of a few cells. The cDRX process would lead to elongated subgrain breakage and grain boundary rotation, which shows
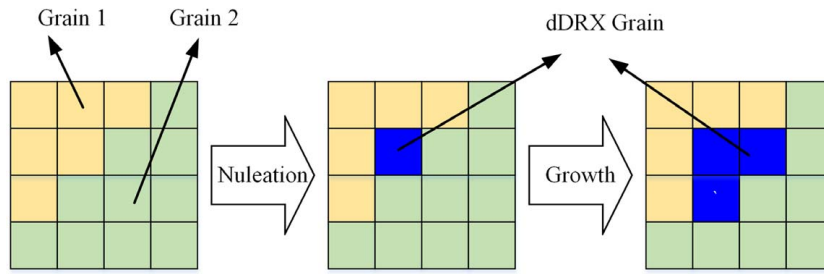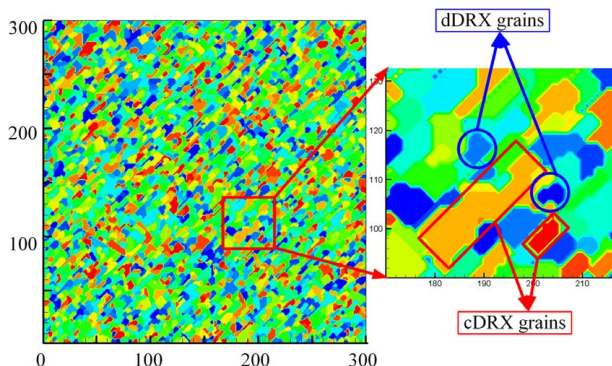
Fig. 9 The status transformation diagram of dDRX process in CA simulation
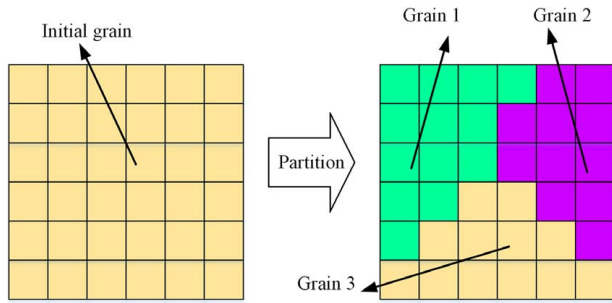
Fig. 10 The status transformation diagram of cDRX process in CA simulation
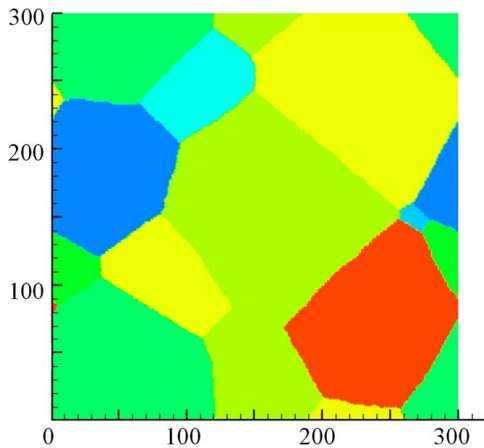
**Fig. 11 The initial grain distribution of CA model**

Fig. 12 The final microstructure simulated by CA model for a cutting speed of 3000 m/min

coarse grains are divided fine grains in CA simulation. Most of the cDRX grains are equiaxed and only a few shows elongated. Note that cDRX nuclei are set at the boundaries of not only initial grains but also dDRX and cDRX grains. Above all, it could be deduced that the dominating mechanism of microstructure evolution during HSM of OFHC copper is a mixed mechanism of dDRX and cDRX.

Figure 13 illustrates microstructure evolution process with the increasing strain ε at different cutting speed (v_c = 750, 1500, 2250, 3000 m/min). At the beginning of simulation, dislocation density is too small to cause grain evolution and grains are still coarse. When the critical dislocation density is reached, nucleation of dDRX and grain division of cDRX occur and considerable microstructure refinement is achieved. Strain increases with the deformation and the effect on grain refinement is more significant. Grains of dDRX grow a little while cDRX continues to happen. Finally, the grain has been fully refined when the given strain value is reached.

Moreover, as the cutting speed increases, the final grain size is further reduced, and the number of grain boundaries is gradually increased. At 750 m/min and 1500 m/min, extremely fine grains are formed by dDRX mechanism because the nuclei do not have enough time to grow. In addition, the grain refinement generated by sub crystalline accumulation and grain boundary rotation is starting to play an important role. Nevertheless, the nucleation rate increases with the increase of strain rate at high cutting speed (v_c = 2250 and 3000 m/min), there are more dDRX grains that nucleate but could not grow. The cDRX process is gradually complete and it is shown that more and more coarse grains are divided into fine grains. In conclusion, with increasing cutting speed, the formation mechanism of fine grains are transformed from dDRX mechanism guiding at relatively low cutting speed to the mixed mechanism of dDRX and cDRX at high cutting speed.

Figure 14 illustrates average grain sizes with the increasing strain at different cutting speeds (v_c = 750, 1500, 2250, 3000 m/min). During microstructure evolution process, the rate of decrease in grain size is very fast at the beginning and then slows down gradually as the increasing of the strain. A large number of subgrains and low angle boundaries are formed by dislocation accumulation. Meanwhile, subgrain size decreases rapidly until it reaches the size corresponding to maximum strain, as a result of high dislocation density under large strain and high strain rate [60]. As shown in Fig. 14, the average grain size is larger at the same strain with higher cutting speed. Higher temperature at higher cutting speed would enhance the annihilation of dislocations and results in slower dislocation generation rate, which leads to larger grain size. The effect of temperature on grain evolution is comparatively complex. On one hand, the dislocation density decreases with the increasing temperature and dynamic recovery and grain growth may occur. On the other hand, the dislocations in the cell boundaries rearrange and neutralize and the dislocation cells translate into subgrains at a certain temperature. High angle boundaries and fine grains are formed with the increase of misorientation angle. It is also shown that the rate of grain size decreasing slows down
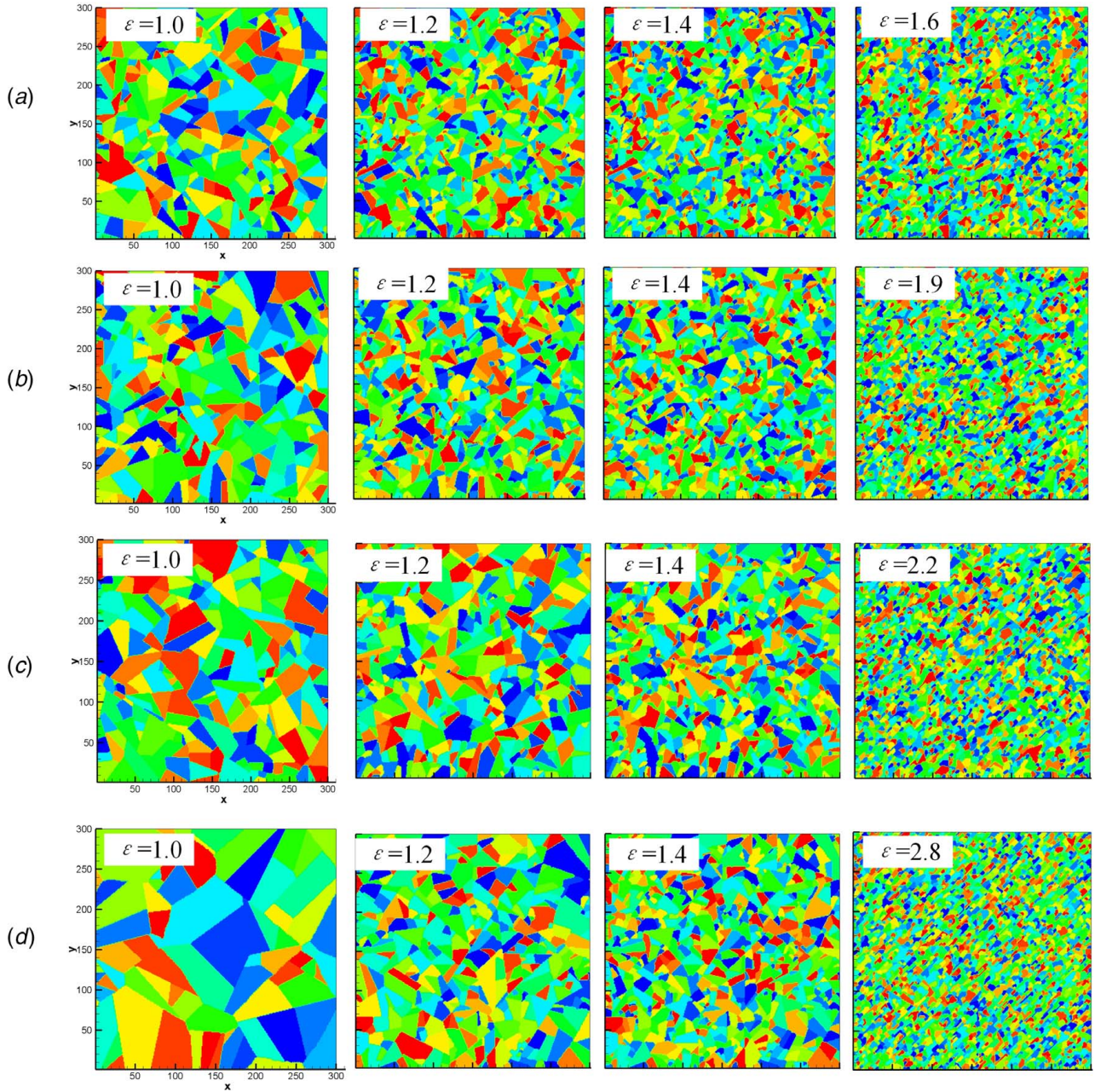
Fig. 13 Simulated microstructure evolution with strain ε at different cutting speeds: (*a*) $v_c = 750$, (*b*) $v_c = 1500$, (*c*) $v_c = 2250$, and (*d*) $v_c = 3000$ m/min

gradually due to a balance between grain refinement and grain growth. In general, the sizes of grains in chip deformation zone have all reached micron scale.
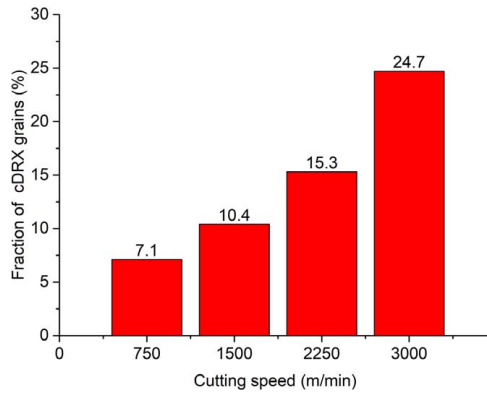
As shown in Fig. 15, the percentage of cDRX grains increases from 7.1% to 24.7% with the cuttitng speed increases from 750 m/min to 3000 m/min. This phenomenon results from high strain rate because the time for the formation of dDRX grains by boundary migration is far longer than that of cDRX grains by boundary rotation. During cutting process, dislocations transfer from the cell interior to its wall due to thermal deformation and lots of dislocation cells with low angle boundaries translate into cDRX grains with high angle. According to finite element results, the strain rate is up to 10^6 and the deformation time is quite short. Therefore, cDRX could meet these characteristics in kinetics and play an important role in microstructure evolution during HSM.

5 Experimental Observation of Microstructure in Chip and Verification of Cellular Automata Model

Figure 16 shows the distributions of grain morphology, size, and misorientation at four different cutting speeds. EBSD images with over 80% resolution are obtained. It can be seen that the grain size is greatly reduced from the initial coarse grain to the fine equiaxed grain. From the EBSD image at different cutting speeds in Fig. 16, it can be seen that larger grains are surrounded by many smaller grains at cutting speed of 750 m/min and 1500 m/min, while more elongated and fine equiaxed grains are observed. Besides that, finer grains can be found at higher cutting speed. It is indicated that grain size reaches micron scale due to the deformation during HSM, which is coincident approximately with simulation results. In the cutting deformation process, grains as elongated along the shear direction and are then refined by
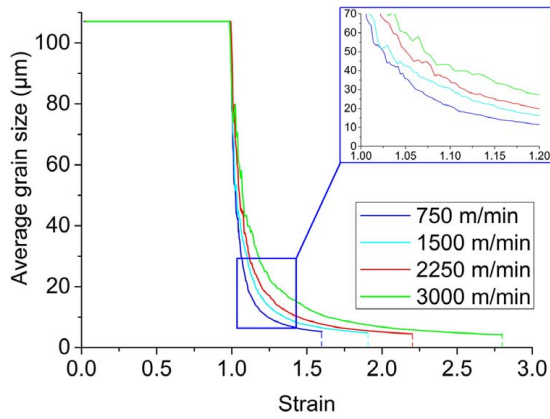
Fig. 14 Evolution of grain sizes with increasing strains at different cutting speeds

Fig. 15 The percentage of the number of cDRX grains at different cutting speeds

DRX under a certain strain rate and temperature. By statistical analysis, most grain sizes are 2–4 μm at 750 m/min and 1500 m/min, while 70% of the grains are less than 2 μm in size at 2250 m/min and 3000 m/min. The grain sizes measured by EBSD are consistent with the simulation results and are both far less than the original size of over 100 μm.

During HSM, many low angle boundaries form in deformation and migrate or rotate inside initial coarse grains, converting to high angle boundaries. At 750 m/min and 1500 m/min, necklace-like structures composed of fine grains around a few wavy boundaries are observed, which explains the main mechanism grain refinement is dDRX. As shown in misorientation distribution of Fig. 16, more low angle boundaries and broken elongated subgrains occur due to high strain rate at 2250 and 3000 m/min, and low angle boundary with less than 15 deg accounts for more than 40%. A large number of low angle boundaries are generated means that the cDRX process becomes more intense, which is beneficial for grain refinement. And then, more high angle boundaries and finer grains are transformed. Above all, it could be deduced that grain refinement can be interpreted in terms of dDRX and cDRX at higher cutting speed.

In this study, the average grain sizes are obtained by the mean linear intercept method. As for the experimental observed EBSD results in Fig. 15, the grain size was measured by using Channel 5 EBSD analysis software. And the CA simulated microstructures in Fig. 11 were analyzed by using an open source MATLAB program "linecut". As shown in Table 10, the results of average grain size from experimental observation and CA simulation are collected and compared. It can be seen from this table that the grains in the chip surface in contact with the tool are severely refined with average size of 2–4 μm, compared with the average initial grains of 100 μm. Moreover, the relative errors between the simulated and experimental observed grain size is less than 7%, which verifies the accuracy of the CA simulation. It can be found that the experimental and simulated results show that the grain size slightly decreases with the increase of cutting speed.

Fig. 16 The distributions of grain morphology, size, and misorientation measured by EBSD at different cutting speeds: (a) 750 m/min, (b) 1500 m/min, (c) 2250 m/min, and (d) 3000 m/min

Table 10 Comparison between experimental and simulated average grain sizes in chips of OFHC at different cutting speeds

v_c (m/min)	CA simulated grain size (μm)	Experimental observed grain size (μm)	Relative error (%)
750	3.48	3.32	4.8
1500	3.12	3.15	0.6
2250	2.88	2.92	1.4
3000	2.52	2.71	7.0

6 Conclusions

In this study, microstructure evolution of OFHC copper during HSM has been thoroughly investigated. The process is modeled using a CA method with DRX mechanism based on the deformation parameters obtained from FE simulation, which has been compared with the cutting experiments and EBSD analysis. It could be concluded as following.

(1) The CA model considering both dDRX and cDRX mechanism was established and the DRX process in the chip during HSM of OFHC copper was simulated. The CA simulation results show well agreement with the experimental observation results, which verifies the feasibility of using CA method to conduct simulation of microstructure evolution in HSM of OFHC copper.

(2) From the CA simulation results, it is identified that the success of CA simulation during HSM of OFHC copper depends on the supplement of cDRX model and deformation parameters (strain, strain rate, and temperature). Due to the addition of the cDRX model, the effect of high strain rate and large deformation on DRX process will be adequately considered. The high strain rate promotes an increasing dislocation density and grain refinement while grain recovery and growth under high temperature will occur, of which this CA model considering both dDRX and cDRX mechanism gives us a further understanding of the refinement process.

(3) The grain refinement mechanism during HSM of OFHC copper was analyzed by comparing the CA simulated and EBSD measured grain sizes. With increasing cutting speed, under the effect of higher strain rate and larger deformation, the dDRX process based on the grain boundary migration theory is inhibited and dDRX grain nuclei does not have enough time to grow so that the mechanism of DRX transforms with the enhance of the cDRX process. As a result, the size of equiaxed grains decreases and more low angle boundaries and deformed substructures are generated, which is thought to result in the evolution of microhardness.

Data Availability Statement

The datasets generated and supporting the findings of this article are obtainable from the corresponding author upon reasonable request. The authors attest that all data for this study are included in the paper. Data provided by a third party listed in Acknowledgements.

References

[1] Rahman, M., Wang, Z. G., and Wong, Y. S., 2006, "A Review on High-Speed Machining of Titanium Alloys," JSME Int. J., Ser. C Mech. Syst. Mach. Elem. Manuf., **49**(1), pp. 11–20.

[2] Dudzinski, D., Devillez, A., Moufki, A., Larrouquère, D., Zerrouki, V., and Vigneau, J., 2004, "A Review of Developments Towards Dry and High Speed Machining of Inconel 718 Alloy," Int. J. Mach. Tools Manuf., **44**(4), pp. 439–456.

[3] Outeiro, J. C., Campocasso, S., Denguir, L. A., Fromentin, G., Vignal, V., and Poulachon, G., 2015, "Experimental and Numerical Assessment of Subsurface Plastic Deformation Induced by OFHC Copper Machining," CIRP Ann. Manuf. Technol., **64**(1), pp. 53–56.

[4] Courbon, C., Mabrouki, T., Rech, J., Mazuyer, D., Perrard, F., and D'Eramo, E., 2014, "Further Insight Into the Chip Formation of Ferritic-Pearlitic Steels: Microstructural Evolutions and Associated Thermo-Mechanical Loadings," Int. J. Mach. Tools Manuf., **77**(1), pp. 34–46.

[5] Arrazola, P. J., Özel, T., Umbrello, D., Davies, M., and Jawahir, I. S., 2013, "Recent Advances in Modelling of Metal Machining Processes," CIRP Ann. Manuf. Technol., **62**(2), pp. 695–718.

[6] M'Saoubi, R., Outeiro, J. C., Chandrasekaran, H., Dillon, O. W., and Jawahir, I. S., 2008, "A Review of Surface Integrity in Machining and Its Impact on Functional Performance and Life of Machined Products," Int. J. Sustain. Manuf., **1**(1–2), pp. 203–236.

[7] Pu, Z., Song, G. L., Yang, S., Outeiro, J. C., Dillon, O. W., Puleo, D. A., and Jawahir, I. S., 2012, "Grain Refined and Basal Textured Surface Produced by Burnishing for Improved Corrosion Performance of AZ31B Mg Alloy," Corros. Sci., **57**, pp. 192–201.

[8] Arisoy, Y. M., and Özel, T., 2015, "Prediction of Machining Induced Microstructure in Ti-6Al-4V Alloy Using 3-D FE-Based Simulations: Effects of Tool Micro-Geometry, Coating and Cutting Conditions," J. Mater. Process. Technol., **220**, pp. 1–26.

[9] Denguir, L. A., Outeiro, J. C., Fromentin, G., Vignal, V., and Besnard, R., 2017, "A Physical-Based Constitutive Model for Surface Integrity Prediction in Machining of OFHC Copper," J. Mater. Process. Technol., **248**(May), pp. 143–160.

[10] Melkote, S. N., Liu, R., Fernandez-Zelaia, P., and Marusich, T., 2015, "A Physically Based Constitutive Model for Simulation of Segmented Chip Formation in Orthogonal Cutting of Commercially Pure Titanium," CIRP Ann. Manuf. Technol., **64**(1), pp. 65–68.

[11] M'Saoubi, R., and Ryde, L., 2005, "Application of the EBSD Technique for the Characterisation of Deformation Zones in Metal Cutting," Mater. Sci. Eng. A, **405**(1–2), pp. 339–349.

[12] Shekhar, S., Cai, J., Wang, J., and Shankar, M. R., 2009, "Multimodal Ultrafine Grain Size Distributions From Severe Plastic Deformation at High Strain Rates," Mater. Sci. Eng. A, **527**(1–2), pp. 187–191.

[13] Huang, Y., and Morehead, M., 2011, "Study of Machining-Induced Microstructure Variations of Nanostructured/Ultrafine-Grained Copper Using XRD," ASME J. Eng. Mater. Technol., **133**(2), p. 021007.

[14] Rancic, M., Colin, C., Sennour, M., Costes, J. P., and Poulachon, G., 2017, "Microstructural Investigations of the White and Deformed Layers Close to the Turned Surface of Ti-6Al-4V," Metall. Mater. Trans. A: Phys. Metall. Mater. Sci., **48**(1), pp. 389–402.

[15] Xu, X., Zhang, J., Liu, H., He, Y., and Zhao, W., 2019, "Grain Refinement Mechanism Under High Strain-Rate Deformation in Machined Surface During High Speed Machining Ti6Al4V," Mater. Sci. Eng. A, **752**, pp. 167–179.

[16] Nie, G.-C., Zhang, K., Outeiro, J., Caruso, S., Umbrello, D., Ding, H., and Zhang, X.-M., 2020, "Plastic Strain Threshold Determination for White Layer Formation in Hard Turning of AISI 52100 Steel Using Micro-Grid Technique and Finite Element Simulations," ASME J. Manuf. Sci. Eng., **142**(3), p. 034501.

[17] Wang, Q., and Liu, Z., 2018, "Microhardness Prediction Based on a Microstructure-Sensitive Flow Stress Model During High Speed Machining Ti-6Al-4V," ASME J. Manuf. Sci. Eng., **140**(9), p. 091003.

[18] Courbon, C., Arrieta, I. M., Cabanettes, F., Rech, J., and Arrazola, P. J., 2020, "The Contribution of Microstructure and Friction in Broaching Ferrite–Pearlite Steels," CIRP Ann., **00**, pp. 4–7.

[19] Cheng, J., and Yao, Y. L., 2002, "Microstructure Integrated Modeling of Multiscan Laser Forming," ASME J. Manuf. Sci. Eng, **124**(2), pp. 379–388.

[20] Estrin, Y., and Kim, H. S., 2007, "Modelling Microstructure Evolution Toward Ultrafine Crystallinity Produced by Severe Plastic Deformation," J. Mater. Sci., **42**(5), pp. 1512–1516.

[21] Ding, H., Shen, N., and Shin, Y. C., 2011, "Modeling of Grain Refinement in Aluminum and Copper Subjected to Cutting," Comput. Mater. Sci., **50**(10), pp. 3016–3025.

[22] Ding, H., and Shin, Y. C., 2014, "Dislocation Density-Based Grain Refinement Modeling of Orthogonal Cutting of Titanium," ASME J. Manuf. Sci. Eng., **136**(4), pp. 1–11.

[23] Tabei, A., Shih, D. S., Garmestani, H., and Liang, S. Y., 2016, "Dynamic Recrystallization of Al Alloy 7075 in Turning," ASME J. Manuf. Sci. Eng., **138**(7), p. 071010.

[24] Behnagh, R. A., Shen, N., Ansari, M. A., Narvan, M., Kazem, M., Givi, B., and Ding, H., 2016, "Experimental Analysis and Microstructure Modeling of Friction Stir Extrusion of Magnesium Chips," ASME J. Manuf. Sci. Eng., **138**(4), p. 041008.

[25] Pan, Z., Liang, S. Y., Garmestani, H., and Shih, D. S., 2016, "Prediction of Machining-Induced Phase Transformation and Grain Growth of Ti-6Al-4 V Alloy," Int. J. Adv. Manuf. Technol., **87**(1–4), pp. 859–866.

[26] Wang, Q., Liu, Z., Wang, B., Song, Q., and Wan, Y., 2016, "Evolutions of Grain Size and Micro-Hardness During Chip Formation and Machined Surface Generation for Ti-6Al-4V in High-Speed Machining," Int. J. Adv. Manuf. Technol., **82**(9–12), pp. 1725–1736.

[27] Imbrogno, S., Rinaldi, S., Umbrello, D., Filice, L., Franchi, R., and Del Prete, A., 2018, "A Physically Based Constitutive Model for Predicting the Surface Integrity in Machining of Waspaloy," Mater. Des., **152**, pp. 140–155.

[28] Goetz, R. L., and Seetharaman, V., 1998, "Modeling Dynamic Recrystallization Using Cellular Automata," Scr. Mater., **38**(3), pp. 405–413.

[29] Ding, R., and Guo, Z. X., 2001, "Coupled Quantitative Simulation of Microstructural Evolution and Plastic Flow During Dynamic Recrystallization," Acta Mater., **49**(16), pp. 3163–3175.

[30] Wang, L., Fang, G., and Qian, L., 2018, "Modeling of Dynamic Recrystallization of Magnesium Alloy Using Cellular Automata Considering Initial Topology of Grains," Mater. Sci. Eng. A, **711**, pp. 268–283.

[31] Li, X., Li, X., Zhou, H., Zhou, X., Li, F., and Liu, Q., 2017, "Simulation of Dynamic Recrystallization in AZ80 Magnesium Alloy Using Cellular Automaton," Comput. Mater. Sci., **140**, pp. 95–104.

[32] Hallberg, H., Wallin, M., and Ristinmaa, M., 2010, "Simulation of Discontinuous Dynamic Recrystallization in Pure Cu Using a Probabilistic Cellular Automaton," Comput. Mater. Sci., **49**(1), pp. 25–34.

[33] Huang, K., and Logé, R. E., 2016, "A Review of Dynamic Recrystallization Phenomena in Metallic Materials," Mater. Des., **111**, pp. 548–574.

[34] Meyers, M. A., Xu, Y. B., Xue, Q., Pérez-Prado, M. T., and McNelley, T. R., 2003, "Microstructural Evolution in Adiabatic Shear Localization in Stainless Steel," Acta Mater., **51**(5), pp. 1307–1325.

[35] Liu, H., Zhang, J., Xu, X., Jiang, Y., He, Y., and Zhao, W., 2017, "Effect of Microstructure Evolution on Chip Formation and Fracture During High-Speed Cutting of Single Phase Metals," Int. J. Adv. Manuf. Technol., **91**(1–4), pp. 823–833.

[36] Buda, J., 1972, "New Methods in the Study of Plastic Deformation in the Cutting Zone," Ann. CIRP, **21**(1), pp. 17–18.

[37] Holmquist, T. J., and Johnson, G. R., 2011, "A Computational Constitutive Model for Glass Subjected to Large Strains, High Strain Rates and High Pressures," ASME J. Appl. Mech., **78**(5), pp. 541–547.

[38] Johnson, G. R., and Cook, W. H., 1985, "Fracture Characteristics of Three Metals Subjected to Various Strains, Strain Rates, Temperatures and Pressures," Eng. Fract. Mech., **21**(1), pp. 31–48.

[39] Mabrouki, T., Girardin, F., Asad, M., and Rigal, J., 2008, "Numerical and Experimental Study of Dry Cutting for an Aeronautic Aluminium Alloy (A2024-T351)," Int. J. Mach. Tools Manuf., **48**(11), pp. 1187–1197.

[40] Zorev, N. N., 1963, "Interrelationship Between Shear Processes Occurring Along Tool Face and on Shear Plane in Metal Cutting," Proc. Int. Res. Prod. Eng. Conf., **49**, pp. 143–152.

[41] Astakhov, V. P., and Shvets, S., 2004, "The Assessment of Plastic Deformation in Metal Cutting," J. Mater. Process. Technol., **146**(2), pp. 193–202.

[42] Samanta, A., Shen, N., Ji, H., Wang, W., Li, J., and Ding, H., 2018, "Cellular Automaton Simulation of Microstructure Evolution for Friction Stir Blind Riveting," ASME J. Manuf. Sci. Eng. Trans. ASME, **140**(3), pp. 1–10.

[43] Cram, D. G., Zurob, H. S., Brechet, Y. J. M., and Hutchinson, C. R., 2009, "Modelling Discontinuous Dynamic Recrystallization Using a Physically Based Model for Nucleation," Acta Mater., **57**(17), pp. 5218–5228.

[44] Mishra, A., Kad, B. K., Gregori, F., and Meyers, M. A., 2007, "Microstructural Evolution in Copper Subjected to Severe Plastic Deformation: Experiments and Analysis," Acta Mater., **55**(1), pp. 13–28.

[45] Hordon, M. J., 1962, "Dislocation Density and Flow Stress of Copper," Acta Metall., **10**(11), pp. 999–1005.

[46] Meyers, M. A., Nesterenko, V. F., LaSalvia, J. C., and Xue, Q., 2001, "Shear Localization in Dynamic Deformation of Materials: Microstructural Evolution and Self-Organization," Mater. Sci. Eng. A, **317**(1–2), pp. 204–225.

[47] Mecking, H., and Kocks, U. F., 1981, "Kinetics of Flow and Strain-Hardening," Acta Metall., **29**(11), pp. 1865–1875.

[48] Won Lee, H., and Im, Y.-K., 2010, "Numerical Modeling of Dynamic Recrystallization During Nonisothermal Hot Compression by Cellular Automata and Finite Element Analysis," Int. J. Mech. Sci., **52**(10), pp. 1277–1289.

[49] Roberts, W., and Ahlblom, B., 1978, "A Nucleation Criterion for Dynamic Recrystallization During Hot Working," Acta Metall., **26**(5), pp. 801–813.

[50] Kugler, G., and Turk, R., 2004, "Modeling the Dynamic Recrystallization Under Multi-Stage hot Deformation," Acta Mater., **52**(15), pp. 4659–4668.

[51] Stüwe, H. P., and Ortner, B. B., 1974, "Recrystallization in Hot Working and Creep," Met. Sci., **8**(1), pp. 161–167.

[52] Qian, M., and Guo, Z. X., 2004, "Cellular Automata Simulation of Microstructural Evolution During Dynamic Recrystallization of an HY-100 Steel," Mater. Sci. Eng. A, **365**(1–2), pp. 180–185.

[53] Estrin, Y., and Vinogradov, A., 2013, "Extreme Grain Refinement by Severe Plastic Deformation: A Wealth of Challenging Science," Acta Mater., **61**(3), pp. 782–817.

[54] Holt, D. L., 1970, "Dislocation Cell Formation in Metals," J. Appl. Phys., **41**(8), pp. 3197–3201.

[55] Chen, F., Qi, K., Cui, Z., and Lai, X., 2014, "Modeling the Dynamic Recrystallization in Austenitic Stainless Steel Using Cellular Automaton Method," Comput. Mater. Sci., **83**, pp. 331–340.

[56] Hall, E. O., 1951, "The Deformation and Ageing of Mild Steel: II Characteristics of the Lüders Deformation," Proc. Phys. Soc. Sect. B, **64**(9), pp. 742–747.

[57] Petch, N. J., 1953, "The Cleavage Strength of Polycrystals," J. Iron Steel Inst., **174**(1), pp. 25–28.

[58] Raabe, D., 1998, *Computational Material Science: The Simulation of Materials, Microstructures and Properties*, Wiley-VCH, Weinheim.

[59] He, Y., Ding, H., Liu, L., and Shin, K., 2006, "Computer Simulation of 2D Grain Growth Using a Cellular Automata Model Based on the Lowest Energy Principle," Mater. Sci. Eng. A, **429**(1–2), pp. 236–246.

[60] Belyakov, A., Sakai, T., Miura, H., and Tsuzaki, K., 2001, "Grain Refinement in Copper Under Large Strain Deformation," Philos. Mag. A Phys. Condens. Matter, Struct. Defects Mech. Prop., **81**(11), pp. 2629–2643.